Chemical Science

ROYAL SOCIETY OF CHEMISTRY

EDGE ARTICLE

View Article Online
View Journal | View Issue

Cite this: *Chem. Sci.*, 2024, **15**, 3928

All publication charges for this article have been paid for by the Royal Society of Chemistry

Received 14th December 2023
Accepted 29th January 2024

DOI: 10.1039/d3sc06705j

rsc.li/chemical-science

Amorphous–crystalline RuTi nanosheets enhancing OH species adsorption for efficient hydrogen oxidation catalysis†

Licheng Wei,[a] Nan Fang,[a] Fei Xue,[a] Shangheng Liu,[a] Wei-Hsiang Huang,[d] Chih-Wen Pao,[d] Zhiwei Hu,[e] Yong Xu, *[c] Hongbo Geng *[b] and Xiaoqing Huang *[a]

Anion exchange membrane fuel cells are a potentially cost-effective energy conversion technology, however, the electrocatalyst for the anodic hydrogen oxidation reaction (HOR) suffers from sluggish kinetics under alkaline conditions. Herein, we report that Ru-based nanosheets with amorphous–crystalline heterointerfaces of Ru and Ti-doped RuO_2 (a/c-Ru/Ti-RuO_2) can serve as a highly efficient HOR catalyst with a mass activity of 4.16 A mg_{Ru}^{-1}, which is 19.8-fold higher than that of commercial Pt/C. Detailed characterization studies show that abundant amorphous–crystalline heterointerfaces of a/c-Ru/Ti-RuO_2 nanosheets provide oxygen vacancies and unsaturated coordination bonds for balancing adsorption of hydrogen and hydroxyl species on Ru active sites to elevate HOR activity. Moreover, Ti doping can facilitate CO oxidation, leading to enhanced strength to CO poisoning. This work provides a strategy for enhancing alkaline HOR performance over Ru-based catalysts with heteroatom and heterointerface dual-engineering, which will attract immediate interest in chemistry, materials science and beyond.

Introduction

Anion exchange membrane fuel cells (AEMFCs) have been regarded as one of the most effective technologies for converting hydrogen fuel to alleviate the current energy crisis and environmental concerns. The mild alkaline conditions of AEMFCs can accommodate more cell components and more durable stability than proton-exchange membrane fuel cells (PEMFCs).[1–4] However, the kinetics of the hydrogen oxidation reaction (HOR) in AEMFCs is two orders of magnitude lower than that in PEMFCs. Under these circumstances, one needs to increase the contents of platinum-group-metals (PGMs) to reach the desired HOR performance, which leads to an increase in cost.[5–7] Moreover, industrial hydrogen produced from the conventional steam reforming process inevitably contains trace amounts of CO, which can poison PGMs during catalysis. Therefore, improving alkaline kinetics, strengthening resistance to CO poisoning, and reducing the loading amounts of PGMs during the HOR are of great importance yet formidably challenging.

Owing to its similar hydrogen affinity to Pt, Ru has been widely recognized as a promising candidate for the HOR. In principle, ideal HOR electrocatalysts should be capable of having appropriate adsorption strengths to H, OH, and CO.[8–10] Optimizing interfaces/surfaces of catalysts to regulate the surface electron structure and reaction energy barrier is the key point for balancing intermediates adsorption.[11–15] Over the past few decades, substantial efforts have been devoted to constructing surface and interfacial synergy for regulating hydrogen binding energy (HBE) and hydroxyl binding energy (OHBE) and thus modulating HOR performance.[12,16,17] Despite great progress in catalyst design for the HOR, high-efficiency HOR electrocatalysis is limited by the sluggish alkaline kinetics and unsatisfactory long-term stability of catalysts. It is of great importance to design efficient electrocatalysts for alkaline HOR yet it is formidably challenging.

Inspired by the significance of amorphous materials with abundant unsaturated sites and defects in catalytic performance,[18–21] here, we synthesize Ru-based nanosheets with amorphous–crystalline heterointerfaces of Ru and Ti-doped RuO_2 (a/c-Ru/Ti-RuO_2) as a highly active and durable catalyst

[a]State Key Laboratory of Physical Chemistry of Solid Surfaces, College of Chemistry and Chemical Engineering, Xiamen University, Xiamen, 361005, China. E-mail: hxq006@xmu.edu.cn

[b]School of Materials Engineering, Changshu Institute of Technology, Changshu, 215500, China

[c]i-Lab Suzhou Institute of Nano-Tech and Nano-Bionics (SINANO), Chinese Academy of Sciences (CAS), 398 Ruoshui Road, Suzhou, 215123, China

[d]National Synchrotron Radiation Research Center, 101 Hsin-Ann Road, Hsinchu 30076, Taiwan

[e]Max Planck Institute for Chemical Physics of Solids, Nothnitzer Strasse 40, Dresden 01187, Germany

† Electronic supplementary information (ESI) available. See DOI: https://doi.org/10.1039/d3sc06705j

for the HOR. Detailed characterization studies show that a/c-Ru/Ti-RuO_2 nanosheets with abundant amorphous–crystalline heterointerfaces provide oxygen vacancies and unsaturated coordination bonds for balancing adsorption of hydrogen and hydroxyl species on Ru active sites to elevate HOR activity. Besides, doping Ti significantly weakened CO adsorption for improving CO tolerance of the a/c-Ru/Ti-RuO_2 catalyst. Impressively, a/c-Ru/Ti-RuO_2 nanosheets exhibit a current density and mass activity of 2.48 mA cm^{-2} and 4.16 A mg_{Ru}^{-1}, respectively, at an overpotential of 50 mV, as well as much superior stability and resistance to CO poisoning to commercial Pt/C.

Results and discussion

a/c-Ru/Ti-RuO_2 was synthesized by mixing ruthenium acetylacetonate and titanium acetylacetonate with a salt template of sodium chloride, which experienced a thermal treatment at 250 °C (Fig. 1a). It was found that a/c-Ru/Ti-RuO_2 exhibited smooth nanosheets with a molar ratio of Ru/Ti of ~3 (Fig. 1b and S1†). The thickness was measured to be ~4.4 nm based on the atomic force microscopy (AFM) result (Fig. 1c). The TEM image and elemental mapping reveal that O, Ru and Ti are uniformly distributed in a/c-Ru/Ti-RuO_2 nanosheets (Fig. 1d and e). HRTEM images show that a/c-Ru/Ti-RuO_2 nanosheets consist of crystalline and amorphous structures with interlaced heterointerfaces (Fig. 1f and S2†). According to fast Fourier-transform (FFT) and inverse fast Fourier-transform (IFFT) images transformed HRTEM of a/c-Ru/Ti-RuO_2 (Fig. 1f and g), the measured lattice distances of 0.227 nm and 0.205 nm correspond to the (111) plane of RuO_2 and (101) plane of Ru, respectively. The diffusion ring without diffraction spots on the FFT image transformed F_2 region confirmed the co-existence of amorphous and crystalline phases on a/c-Ru/Ti-RuO_2 (Fig. 1h), which was further validated by XRD. Based on the XRD and HRTEM images (Fig. S3 and S4†), the crystal structure and

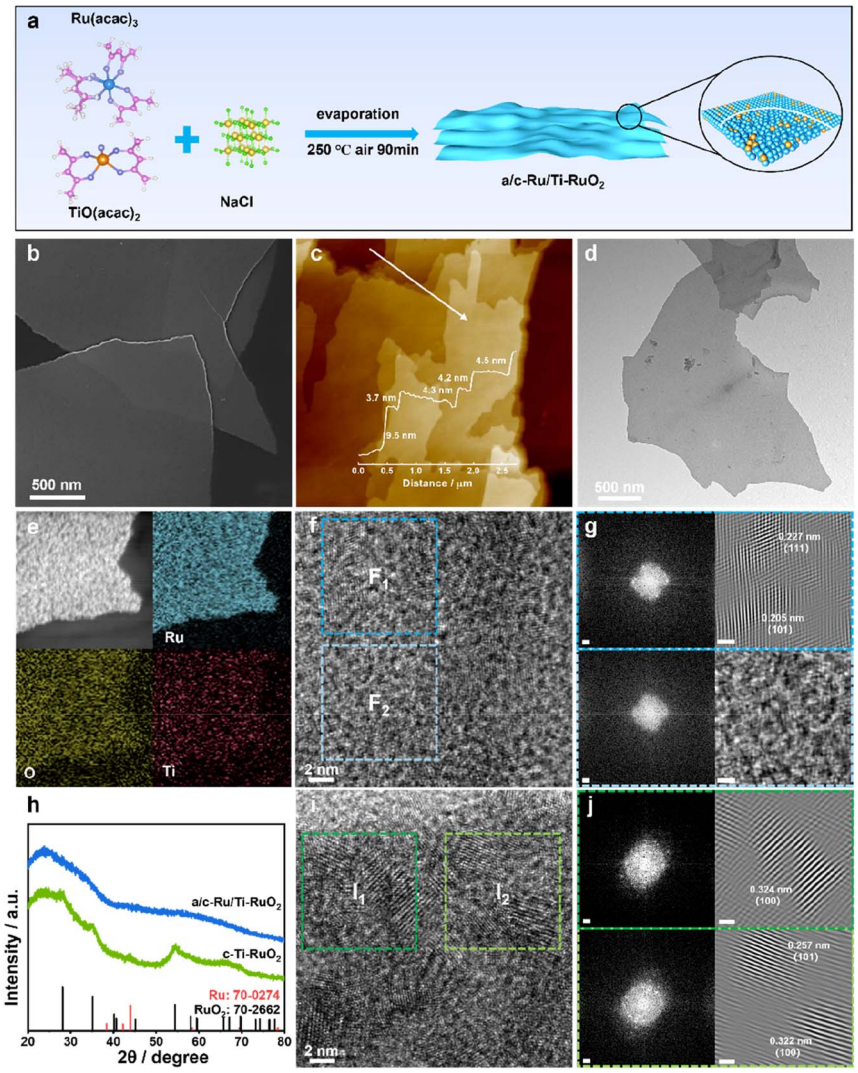

Fig. 1 (a) Schematic illustration for the synthesis of a/c-Ru/Ti-RuO_2 nanosheets. (b) SEM, (c) AFM, (d) TEM, (e) elemental mapping, and (f) HRTEM image of a/c-Ru/Ti-RuO_2. (g) FFT and IFFT images transformed from (f). (h) XRD patterns of a/c-Ru/Ti-RuO_2 and c-Ti-RuO_2. (i) HRTEM image of c-Ti-RuO_2. (j) FFT and IFFT images transformed from (i). The scale bars in FFT and IFFT images are 1/2 nm and 1 nm, respectively.

morphology of a/c-Ru/RuO_2 is similar to those of a/c-Ru/Ti-RuO_2. The lattice distances of 0.205 nm, 0.214 nm, and 0.222 nm in the HRTEM image of a/c-Ru/RuO_2 can be indexed as the (101) and (002) planes of metallic Ru and (110) plane of RuO_2, respectively. Note that the lattice distance of RuO_2 (0.227 nm) in the HRTEM image of a/c-Ru/Ti-RuO_2 is larger than that in a/c-Ru/RuO_2 (0.222 nm), which can be ascribed to the lattice expansion of RuO_2 after Ti doping. Moreover, crystalline Ti doped Ru nanosheets and Ru nanosheets, which were named c-Ti-RuO_2 and c-RuO_2, respectively, were prepared by increasing synthetic temperature to 300 °C (see the ESI† for details). In the XRD of c-Ti-RuO_2 nanosheets, the peaks at 28.0°, 35.3°, and 54.4° are indexed to the (110), (101), and (211) planes of RuO_2, respectively (Fig. 1h and S5,† PDF: 70-2662). Comparing with c-RuO_2, the peak of the (110) plane in the XRD pattern of c-Ti-RuO_2 negatively shifts by 0.26°, implying that doping of Ti onto RuO_2 induces the formation of lattice expansion.[22] Despite the similar morphology, agglomerated nanoparticles appear on c-Ti-RuO_2 nanosheets due to the increase in temperature during synthesis (Fig. S6†). Moreover, the HRTEM image and FFT and IFFT images of c-Ti-RuO_2 further indicate that c-Ti-RuO_2 is mainly composed of interlaced crystalline heterointerfaces. The lattice distances of 0.324 nm, 0.257 nm and 0.322 nm in the HRTEM image of c-Ti-RuO_2 are ascribed to the (110), (101) and (110) planes of RuO_2, respectively (Fig. 1i and j). Note that the lattice distance of the (110) plane for c-Ti-RuO_2 is larger than that of RuO_2 (0.317 nm), further confirming lattice expansion after Ti doping, which is consistent with the XRD results.

To investigate the effects of Ti doping on a/c-Ru/Ti-RuO_2 with amorphous–crystalline heterointerfaces, electron paramagnetic resonance (EPR) spectroscopy was performed.[23] As shown in Fig. 2a and S7,† it was found that Ti doping and the amorphous–crystalline heterointerface both contribute to the formation of oxygen vacancies. Moreover, the surface electronic properties of a/c-Ru/Ti-RuO_2 and c-Ti-RuO_2 were measured by XPS (Fig. S8†). It was noted that Ru consists of Ru^0 and Ru^{4+} in a/c-Ru/Ti-RuO_2 and c-Ti-RuO_2 (Fig. 2b). Compared to c-Ti-RuO_2, the position of Ru^{4+} in the XPS spectrum of a/c-Ru/Ti-RuO_2 negatively shifted by 0.12 eV, which was attributed to the amorphous structure of metallic Ru^0.[24,25] A similar negative shift was observed for the Ti 2p peak (Fig. 2c) in the XPS spectra of a/c-Ru/Ti-RuO_2, which could be attributed to the formation of oxygen vacancies and the amorphous–crystalline heterointerface.[23,26,27] In O 1s XPS spectra, the peaks at 529.6 eV, 530.6 eV and 532.5 eV were ascribed to Ru–O/Ti–O, surface bridge oxide of RuO_2 (Ru–O_{BRI}) and OH species on coordinatively unsaturated Ru sites (Ru–O_{CUS}), respectively (Fig. 2d).[28] Moreover, the larger amounts of Ru–O_{BRI} in a/c-Ru/Ti-RuO_2 compared with c-Ti-RuO_2 confirmed more oxygen vacancy formation in a/c-Ru/Ti-RuO_2 (Table S1†), which was in line with the EPR results.

Furthermore, X-ray absorption near-edge structure spectroscopy (XANES) was performed to investigate the electronic structures of a/c-Ru/Ti-RuO_2 and c-Ti-RuO_2. Compared to RuO_2, the smaller energy shift of the Ru-K edge position suggested that the valence of Ru in a/c-Ru/Ti-RuO_2 and c-Ti-RuO_2 is slightly lower than that in RuO_2 (Fig. 2e). Compared to c-Ti-RuO_2, the Ru-K edge of a/c-Ru/Ti-RuO_2 slightly shifted to lower energy, suggesting that the amorphous structure of metallic Ru and the formation of oxygen vacancies in a/c-Ru/Ti-RuO_2 influenced the electronic properties of Ru. In the corresponding Fourier-transformed extended X-ray absorption fine structure spectroscopy (EXAFS) spectra, the peaks at 1.47 Å and 3.10 Å in Ru–K EXAFS spectra were ascribed to the first Ru–O and second Ru–Ru coordination of RuO_2, respectively, while the peak at 2.39 Å represented the Ru–Ru coordination of Ru foil (Fig. 2f). Compared to c-Ti-RuO_2, the lower peak intensity of Ru–O coordination in the EXAFS spectrum of a/c-Ru/Ti-RuO_2 compared with that of RuO_2 implied unsaturated Ru–O coordination due to the formation of oxygen vacancies in a/c-Ru/Ti-RuO_2.[29–31] Furthermore, the feature at 3.01 Å was ascribed to Ru–Ti coordination in c-Ti-RuO_2 (Fig. 2f). Compared to c-Ti-RuO_2 (~3.01 Å), the peak of Ru–Ti coordination in the EXAFS spectrum of a/c-Ru/Ti-RuO_2 shifted to shorter distance and obviously weakened, indicating the higher disorder degree of a/c-Ru/Ti-RuO_2 (Fig. 2f), which was further confirmed by the wavelet transformation (WT) contour plots (Fig. 2g). In addition, the absence of Ru–Ru coordination in the EXAFS spectrum of a/c-Ru/Ti-RuO_2 may be caused by the disorder structure and small proportion of metallic Ru.[29]

HOR performance was performed using a typical three-electrode system on a rotating disk electrode (RDE) with H_2-saturated alkaline electrolyte (0.1 M KOH). All electrochemical performance of catalysts was tested after activating for 100 cycles at a scan rate of 0.5 V s^{-1} at potential from −0.2 to 0.4 V *vs.* RHE. Screening experiments suggested that a/c-Ru/Ti-RuO_2 with a Ru/Ti ratio of 3 : 1 was the optimal HOR catalyst (Fig. S9†). Furthermore, the HOR polarization curve of a/c-Ru/Ti-RuO_2 tested N_2-saturated 0.1 M KOH solution (Fig. S10†) showed that current density is close to zero, indicating the occurrence of the HOR in H_2-saturated 0.1 M KOH solution. As shown in Fig. 3a, a/c-Ru/Ti-RuO_2 exhibited a current density of 2.48 mA cm^{-2} at 50 mV, which was higher than that of c-Ti-RuO_2 (1.54 mA cm^{-2}) and a/c-Ru/RuO_2 (2.00 mA cm^{-2}), indicating that the amorphous–crystalline heterointerface and Ti doping synergistically improved alkaline HOR activity. Moreover, the HOR polarization curves of catalysts were collected at different rotating rates from 400 to 2500 rpm to analyse the electron transport process (Fig. 3b and S11a–c†). The fitting slopes in Koutecky–Levich plots of a/c-Ru/Ti-RuO_2, a/c-Ru/RuO_2, c-Ti-RuO_2, and Pt/C (inset of Fig. 3b and S11d†) were 13.83, 13.49, 14.86, and 14.79 cm^2 mA^{-1} $rpm^{1/2}$, respectively, showing limiting current densities of 2.89, 2.96, 2.69, and 2.70 mA cm^{-2} at 1600 rpm, being consistent with the theoretical value.[32] The kinetic currents (i_k) were calculated by Butler–Volmer fitting. a/c-Ru/Ti-RuO_2 displayed higher kinetic current than the other catalysts at all potentials, suggesting its fastest HOR kinetics (Fig. 3c). The exchange current (i_0) of a/c-Ru/Ti-RuO_2, which was calculated *via* the Butler–Volmer equation with nonlinear fitting, was 1.49 mA, which was 3.6, 1.9, and 5.3 times compared with that of c-Ti-RuO_2 (0.42 mA), a/c-Ru/RuO_2 (0.77 mA), and commercial Pt/C (0.28 mA). To quantitatively compare HOR activity, the mass activity and specific activity of these catalysts were normalized to the mass of Ru or Pt and electrochemically surface area (ECSA, marked as $j^{k,m}$ and $j^{0,s}$). The loading mass of Ru was measured by thermogravimetry (TG) and energy dispersive spectroscopy (EDS)

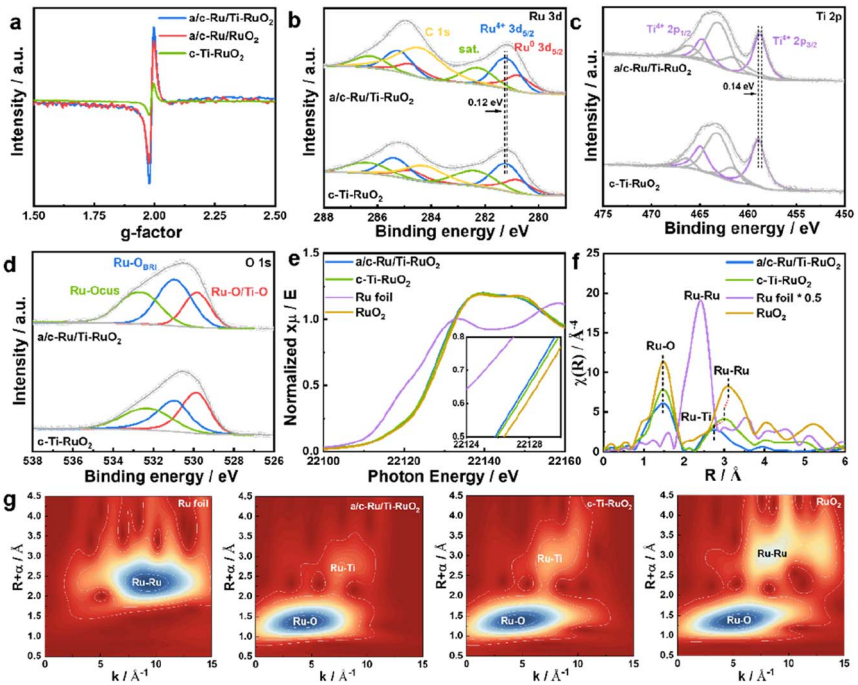

Fig. 2 (a) EPR spectra of a/c-Ru/RuO_2, a/c-Ru/Ti-RuO_2 and c-Ti-RuO_2. (b–d) Ru 3d, Ti 2p and O 1s spectra of a/c-Ru/Ti-RuO_2 and c-Ti-RuO_2. (e) Normalized XANES spectra of Ru foil, a/c-Ru/Ti-RuO_2, c-Ti-RuO_2, and RuO_2 at the Ru-K edge. (f) The Fourier-transform (FT) k^3-weighted $\chi(k)$ function of the EXAFS spectra of Ru foil, a/c-Ru/Ti-RuO_2, c-Ti-RuO_2, and RuO_2 at the Ru-K edge. (g) Wavelet transformation for the k^3-weighted EXAFS of the Ru-K edge for Ru foil, a/c-Ru/Ti-RuO_2, c-Ti-RuO_2, and RuO_2.

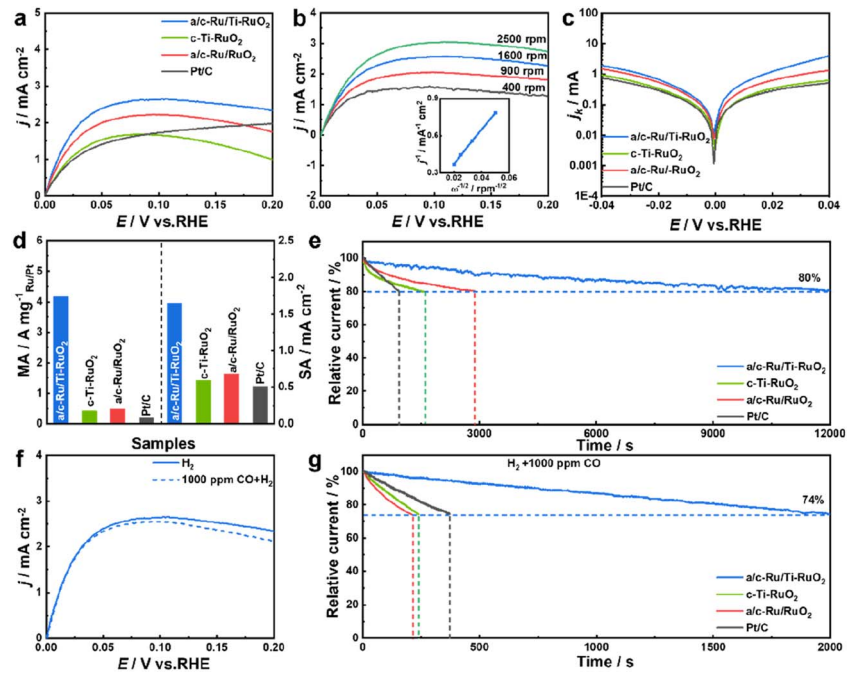

Fig. 3 (a) HOR polarization curves of a/c-Ru/Ti-RuO_2, c-Ti-RuO_2, a/c-Ru/RuO_2 and commercial Pt/C. (b) HOR polarization curves of a/c-Ru/Ti-RuO_2 at different rotating speeds (inset: Koutecky–Levich plots of the catalyst at 0.1 V *vs.* RHE). (c) Tafel plots and (d) kinetic current density and exchange current density for various catalysts. (e) Chronoamperometric responses at an overpotential of 0.1 V *vs.* RHE of catalysts in H_2-saturated 0.1 M KOH. (f) HOR polarization curves of a/c-Ru/Ti-RuO_2 in H_2-saturated and 1000 CO ppm + H_2-saturated 0.1 M KOH electrolyte. (g) Chronoamperometric responses at an overpotential of 0.1 V *vs.* RHE of catalysts in 1000 CO ppm + H_2-saturated 0.1 M KOH electrolyte.

(Fig. S1, S6 and S12†). As shown in Fig. 3d, the $j^{k,m}$ of a/c-Ru/Ti-RuO_2 was 4.16 A mg_{Ru}^{-1}, which was 9.2, 7.7, and 19.8 times higher than that of c-Ti-RuO_2 (0.41 A mg_{Ru}^{-1}), a/c-Ru/RuO_2 (0.48 A mg_{Ru}^{-1}), and commercial Pt/C (0.20 A mg_{Pt}^{-1}), respectively. Note that the mass activity of a/c-Ru/Ti-RuO_2 has surpassed that of most reported catalysts (Fig. S13 and Table S2†). Moreover, ECSAs were obtained by Cu underpotential deposition (Cu_{UPD}) stripping (Fig. S14†). Then, ECSA normalized specific activities of a/c-Ru/Ti-RuO_2, c-Ti-RuO_2, a/c-Ru/RuO_2 and commercial Pt/C were 1.65, 0.59, 0.68, and 0.51 mA cm^{-2}, respectively. The highest mass activity and specific activity of a/c-Ru/Ti-RuO_2 indicated the best kinetic and intrinsic activities of a/c-Ru/Ti-RuO_2. Furthermore, the stability of catalysts was tested in H_2-saturated 0.1 M KOH electrolyte by chronoamperometry technology at 0.1 V *vs.* RHE. a/c-Ru/Ti-RuO_2 could maintain 80% of the initial current after stability testing for 12 000 s, which was much longer than that for a/c-Ru/RuO_2 (2900 s), c-Ti-RuO_2 (1560 s), and Pt/C (940 s) (Fig. 3e). Specifically, the morphology of a/c-Ru/Ti-RuO_2 was well maintained with only negligible Ru dissolution after durability testing (Fig. S15†).

In addition, the resistance to CO poisoning of a/c-Ru/Ti-RuO_2 was tested by introducing 1000 ppm CO (Fig. 3f). A slight decline in the HOR polarization curve of a/c-Ru/Ti-RuO_2 was observed in 1000 ppm CO + H_2-saturated 0.1 M KOH electrolyte, which was much smaller than that of c-Ti-RuO_2, a/c-Ru/RuO_2, and commercial Pt/C (Fig. S16†), indicating that Ti doping and the heterointerface efficiently block CO species from poisoning active sites. Besides, the superior resistance of a/c-Ru/Ti-RuO_2 to CO poisoning was further evaluated by chronoamperometry at 0.1 V *vs.* RHE. As shown in Fig. 3g, the currents of c-Ti-RuO_2, a/c-Ru/RuO_2, and commercial Pt/C sharply decreased to 74% of the initial current after being tested for 240 s, 210 s, and 370 s, respectively, while 74% of the initial current was maintained after 2000 s for a/c-Ru/Ti-RuO_2, indicating the superior CO tolerance of a/c-Ru/Ti-RuO_2 to other references.

To deeply understand the enhanced HOR performance over a/c-Ru/Ti-RuO_2, CV, *in situ* FTIR, H/D isotope experiment and CO stripping experiment were performed. The larger area of the CV curve of a/c-Ru/Ti-RuO_2 than that of c-Ti-RuO_2 and a/c-Ru/RuO_2 implied that more active sites were exposed on a/c-Ru/Ti-RuO_2 (Fig. S17†). The intense peak, appearing at ~0.1 V *vs.* RHE in the CV curve after activating for 100 cycles, corresponded to the adsorption of hydrogen and exchange reaction of hydrogen to adsorbed hydroxyl, which contributed to exposure of active sites of a/c-Ru/Ti-RuO_2 after activation (Fig. 4a).[7] Note that the morphology and structure of a/c-Ru/Ti-RuO_2 were largely preserved after the present activation (Fig. S18a–d†). In XPS spectra, the positive shift of the Ru 3d peak for a/c-Ru/Ti-RuO_2 after activation was attributed to the adsorption of OH_{ad} species in alkaline electrolyte (Fig. S18e†),[33–35] which was further confirmed by the positive shifts of Ru–O_{CUS} and Ru–O_{BRI} peaks in the XPS spectrum of activated a/c-Ru/Ti-RuO_2 (Fig. 4b).[36–38] The new peak at 535.3 eV was ascribed to the O–F bond due to the Nafion binder. Analysis of XANES and EXAFS spectra of the fresh and activated a/c-Ru/Ti-RuO_2 further confirmed that the present activation could significantly enhance OH_{ad} adsorption, due to lower coordination of Ru–Ru after activation than fresh a/c-Ru/Ti-RuO_2 (Fig. 4c and S18f†). Furthermore, based on comparison CV curves of catalysts after activating for 100 cycles, the larger oxidation peak area of a/c-Ru/Ti-RuO_2 than that of c-Ti-RuO_2, a/c-Ru/RuO_2, and commercial Pt/C suggested stronger interaction between Ru and hydrogen/hydroxyl species, while the lower potential in the CV peak further indicated its weak binding ability with adsorbed hydrogen (Fig. 4a, d and S19†). This is due to the optimized electronic structure of Ru active sites by oxygen vacancies and unsaturated coordination of a/c-Ru/Ti-RuO_2 with amorphous–crystallines interface. Moreover, an isotope experiment was performed to further evaluate the enhanced OH_{ad} adsorption.[8,39] As shown in Fig. S20,† the decreased current density ratio of j_{KOH}/j_{KOD} with potential implies that the replacement of OH^- with OD^- reduces the HOR activity of catalysts, which is attributed to the different pD/pH values of KOD and KOH.[40,41] Note that the ratio of j_{KOH}/j_{KOD} for a/c-Ru/Ti-RuO_2 is much smaller than that of commercial Pt/C, indicating its strong adsorption ability towards both OH^- and OD^- on a/c-Ru/Ti-RuO_2, as a result of significantly enhanced HOR performance of a/c-Ru/Ti-RuO_2 (Fig. 4e).[42]

Besides, *in situ* Fourier transform infrared spectroscopy (FTIR) was performed in H_2-saturated 0.1 M KOH electrolyte to evaluate the HBE and OHBE for a/c-Ru/Ti-RuO_2. As shown in Fig. S21,† a vibrational band is observed at 2064 cm^{-1} for a/c-RuTi, which is ascribed to the Ru–H bond.[7] Note that the Ru–H vibration of a/c-Ru/Ti-RuO_2 negatively shifts to a lower wavenumber compared with that of c-Ti-RuO_2 (2071 cm^{-1}), suggesting that the binding strength of H on a/c-Ru/Ti-RuO_2 is weaker than that on c-Ti-RuO_2.[43,44] The band at ~3400 cm^{-1} in *in situ* FTIR spectra was ascribed to O–H stretching vibration of interfacial water,[7,45,46] where a larger Stark tuning rate for a/c-Ru/Ti-RuO_2 (−100 cm^{-1} V^{-1}) than that of c-Ti-RuO_2 (−74 cm^{-1} V^{-1}) indicates that the heterointerface of a/c-Ru/Ti-RuO_2 is beneficial to enhance interaction with OH_{ad} species (Fig. 4f).[45] Additionally, a CO-stripping experiment was performed to reveal the enhanced resistance to CO poisoning of a/c-Ru/Ti-RuO_2. As shown in Fig. 4g and S22,† the peak potential of CO stripping follows the trend as a/c-Ru/Ti-RuO_2 (0.689 V *vs.* RHE) < c-Ti-RuO_2 (0.702 V *vs.* RHE) < a/c-Ru/RuO_2 (0.718 V *vs.* RHE), suggesting that Ti doping efficiently enhances OH species affinity of a/c-Ru/RuO_2 for facilitating adsorbed CO oxidation. In the *in situ* FTIR spectra collected from −0.15 to 1.05 V *vs.* RHE, the adsorption peaks at ~2094 cm^{-1} and ~1850 cm^{-1} could be assigned to CO linear and bridged adsorption, respectively (Fig. 4h).[47–50] Compared to a/c-Ru/RuO_2, the absence of the peak of CO bridged adsorption in FTIR spectra of a/c-Ru/Ti-RuO_2 and c-Ti-RuO_2 suggests that Ti-doping can weaken CO adsorption.[47] Besides, the peak intensity of CO linear adsorption for a/c-Ru/Ti-RuO_2 and c-Ti-RuO_2 decreases much faster than that of a/c-Ru/RuO_2 with the potentials, further confirming the weakened CO adsorption on a/c-Ru/Ti-RuO_2 and c-Ti-RuO_2.[51,52] In addition, the peak of CO adsorption completely disappears at 0.65 V *vs.* RHE in the *in situ* FTIR spectrum of a/c-Ru/Ti-RuO_2, while the obvious peaks of CO adsorption in the FTIR spectra of a/c-Ru/RuO_2 at the same potential demonstrate that the strong synergy at the heterointerface can significantly weaken the binding strength of CO on a/c-Ru/Ti-RuO_2 (Fig. S23†). Based on the above results, the

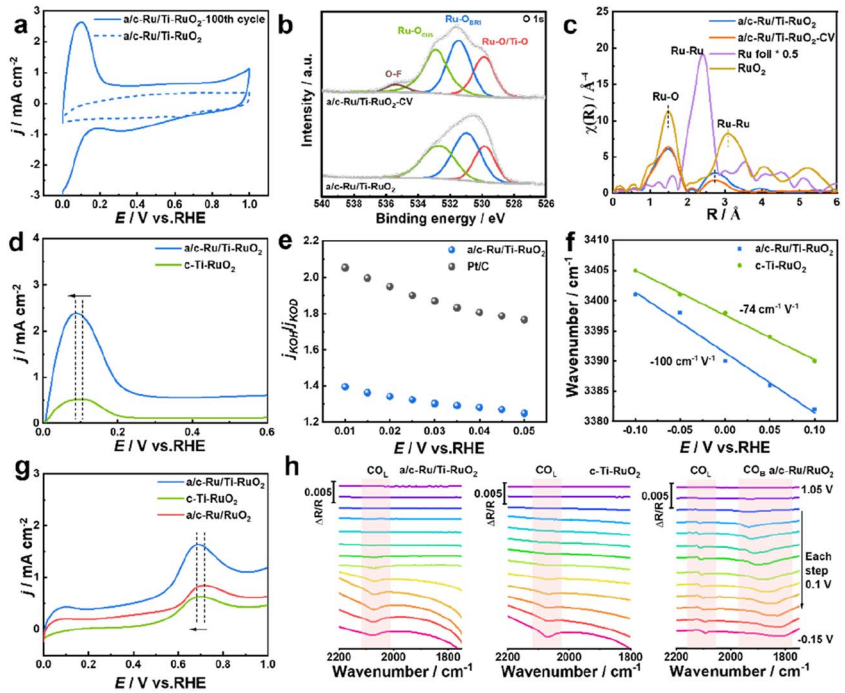

Fig. 4 (a) CV curves collected in 0.1 M KOH during 0–1 V *vs.* RHE of a/c-Ru/Ti-RuO_2 before and after activating for 100 cycles. (b) O 1s spectra and (c) Ru K-edge Fourier-transform (FT) k^3-weighted $\chi(k)$ function of the EXAFS spectra of a/c-Ru/Ti-RuO_2 before and after CV activation. (d) CV peaks of a/c-Ru/Ti-RuO_2 and c-Ti-RuO_2 in 0.1 M KOH. (e) The ratio of current density in 0.1 M KOH and KOD electrolyte for a/c-Ru/Ti-RuO_2 and commercial Pt/C. (f) *In situ* FTIR wavenumber change of O–H stretching vibration for a/c-Ru/Ti-RuO_2 and c-Ti-RuO_2. (g) CO-stripping voltammetry of a/c-Ru/Ti-RuO_2, c-Ti-RuO_2, and a/c-Ru/RuO_2. (h) *In situ* FTIR spectra of a/c-Ru/Ti-RuO_2, c-Ti-RuO_2, and a/c-Ru/RuO_2 for CO oxidation recorded during stepping the potential from −0.15 to 1.05 V *vs.* RHE in 0.1 M KOH electrolyte.

amorphous–crystalline heterointerface is beneficial for formation of oxygen vacancies, which can weaken binding energy of Ru–H and promote OH_{ad} adsorption, as a result of improved HOR performance.

Conclusions

In summary, we have demonstrated that a/c-Ru/Ti-RuO_2 nanosheets can serve as an efficient catalyst for alkaline HOR. The results from XAFS, the isotopic experiment, and *in situ* FTIR suggest that the amorphous–crystalline heterointerface of a/c-Ru/Ti-RuO_2 provides abundant oxygen vacancies, which can weaken binding energy of Ru–H and strengthen OH_{ad} adsorption, leading to a significant enhancement in alkaline HOR activity. Impressively, the mass activity and specific activity of a/c-Ru/Ti-RuO_2 reach 4.16 A mg_{Ru}^{-1} and 1.65 mA cm^{-2}, which are 19.8 times and 2.2 times higher than that of commercial Pt/C, respectively. Moreover, a/c-Ru/Ti-RuO_2 with amorphous–crystalline heterointerfaces displays fast CO oxidation efficiently enhancing its CO tolerance. This work provides a strategy for enhancing alkaline HOR performance over Ru-based catalysts, which will attract immediate interest in chemistry, materials science and beyond.

Data availability

The data supporting the findings of this study, including chemicals, sample preparation, instrumentation, supplementary tests, and corresponding supplementary discussions, are available in ESI.†

Author contributions

Licheng Wei: conceptualization, methodology, validation, formal analysis, investigation, writing – original draft, visualization. Nan Fang, Fei Xue, Shangheng Liu, Wei-Hsiang Huang, Chih-Wen Pao, Zhiwei Hu: formal analysis, investigation. Yong Xu: writing – review & editing, supervision. Hongbo Geng: writing – review & editing, supervision, funding acquisition. Xiaoqing Huang: conceptualization, resources, writing – review & editing, supervision, project administration, funding acquisition.

Conflicts of interest

There are no conflicts to declare.

Acknowledgements

This work was financially supported by the National Key R&D Program of China (2020YFB1505802), the Ministry of Science and Technology of China (2017YFA0208200), the National Natural Science Foundation of China (22025108, U21A20327, and 22121001), the start-up support from Xiamen University, the Natural Science Foundation of the Jiangsu Higher Education Institutions (22KJA430009), the Science and Technology Development Plan of Suzhou (ZXL2022176), and the

Guangdong Provincial Natural Science Fund for Distinguished Young Scholars (2021B1515020081). We acknowledge support from the Max Planck-POSTECH-Hsinchu Center for Complex Phase Materials.

Notes and references

1 X. Wang, X. Li, D. Kong, L. Zhao, Y. Cui, Y. Wang, T. Cai, Q. Xue, Z. Yan and W. Xing, *Nano Energy*, 2022, **104**, 107877.
2 L. Su, D. Gong, Y. Jin, D. Wu and W. Luo, *J. Energy Chem.*, 2022, **66**, 107–122.
3 W. Moschkowitsch, O. Lori and L. Elbaz, *ACS Catal.*, 2022, **12**, 1082–1089.
4 J. R. Varcoe and R. C. T. Slade, *Fuel Cells*, 2005, **5**, 187–200.
5 D. Strmcnik, M. Uchimura, C. Wang, R. Subbaraman, N. Danilovic, D. van der Vliet, A. P. Paulikas, V. R. Stamenkovic and N. M. Markovic, *Nat. Chem.*, 2013, **5**, 300–306.
6 Y. Wang, G. Wang, G. Li, B. Huang, J. Pan, Q. Liu, J. Han, L. Xiao, J. Lu and L. Zhuang, *Energy Environ. Sci.*, 2015, **8**, 177–181.
7 Y. Xue, L. Shi, X. Liu, J. Fang, X. Wang, B. P. Setzler, W. Zhu, Y. Yan and Z. Zhuang, *Nat. Commun.*, 2020, **11**, 5651.
8 B. Zhang, B. Zhang, G. Zhao, J. Wang, D. Liu, Y. Chen, L. Xia, M. Gao, Y. Liu, W. Sun and H. Pan, *Nat. Commun.*, 2022, **13**, 5894.
9 L. Su, Y. Zhao, Y. Jin, Z. Liu, H. Cui and W. Luo, *Adv. Funct. Mater.*, 2022, **32**, 2113047.
10 T. Wang, L. Y. Li, L. N. Chen, T. Sheng, L. Chen, Y. C. Wang, P. Zhang, Y. H. Hong, J. Ye, W. F. Lin, Q. Zhang, P. Zhang, G. Fu, N. Tian, S. G. Sun and Z. Y. Zhou, *J. Am. Chem. Soc.*, 2022, **144**, 9292–9301.
11 L. Zhang, H. Jang, H. Liu, M. G. Kim, D. Yang, S. Liu, X. Liu and J. Cho, *Angew. Chem., Int. Ed.*, 2021, **60**, 18821–18829.
12 F. Yang, X. Bao, P. Li, X. Wang, G. Cheng, S. Chen and W. Luo, *Angew. Chem., Int. Ed.*, 2019, **58**, 14179–14183.
13 L. Su, Y. Jin, D. Gong, X. Ge, W. Zhang, X. Fan and W. Luo, *Angew. Chem., Int. Ed.*, 2023, **62**, e202215585.
14 W. Wang, S. Guo, I. Lee, K. Ahmed, J. Zhong, Z. Favors, F. Zaera, M. Ozkan and C. S. Ozkan, *Sci. Rep.*, 2014, **4**, 4452.
15 J. Xu and X. Kong, *Small Methods*, 2022, **6**, e2101432.
16 M. Kundu, R. Mishra, T. Bhowmika and S. Barman, *J. Mater. Chem. A*, 2018, **6**, 23531–23541.
17 Y. Yang, X. Sun, G. Han, X. Liu, X. Zhang, Y. Sun, M. Zhang, Z. Cao and Y. Sun, *Angew. Chem., Int. Ed.*, 2019, **58**, 10644–10649.
18 Y. Zhou, W. Hao, X. Zhao, J. Zhou, H. Yu, B. Lin, Z. Liu, S. J. Pennycook, S. Li and H. J. Fan, *Adv. Mater.*, 2022, **34**, e2100537.
19 Y. Zhang, J. Fang, L. Zhang, D. Wei, W. Zhu and Z. Zhuang, *Chem. Commun.*, 2022, **58**, 4488–4491.
20 Z. Ma, C. Chen, X. Cui, L. Zeng, L. Wang, W. Jiang and J. Shi, *ACS Appl. Mater. Interfaces*, 2021, **13**, 44224–44233.
21 J. Kang, G. Liu, Q. Hu, Y. Huang, L.-M. Liu, L. Dong, G. Teobaldi and L. Guo, *J. Am. Chem. Soc.*, 2023, **145**, 25143–25149.
22 J. Zhang, G. Ren, D. Li, Q. Kong, Z. Hu, Y. Xu, S. Wang, L. Wang, M. Cao and X. Huang, *Sci. Bull.*, 2022, **67**, 2103–2111.
23 J. Kang, X. Qiu, Q. Hu, J. Zhong, X. Gao, R. Huang, C. Wan, L. M. Liu, X. Duan and L. Guo, *Nat. Catal.*, 2021, **4**, 1050–1058.
24 A. Foelske, O. Barbieri, M. Hahn and R. Kötz, *Electrochem. Solid-State Lett.*, 2006, **9**, 268–272.
25 S. Liu, L. Dai, Y. Qu, Y. Qiu, J. Fan, X. Li, Q. Zhangc and X. Guo, *Mater. Chem. Front.*, 2021, **5**, 6648–6658.
26 G. Feng, M. Hu, S. Yuan, J. Nan and H. Zeng, *Nanomaterials*, 2021, **11**, 2801.
27 J. Xu, W. Dong, C. Song, Y. Tang, W. Zhao, Z. Hong and F. Huang, *J. Mater. Chem. A*, 2016, **4**, 15698–15704.
28 J. P. Zheng, P. J. Cygan and T. R. Jow, *J. Electrochem. Soc.*, 1995, **142**, 2699–2703.
29 G. Wu, X. Zheng, P. Cui, H. Jiang, X. Wang, Y. Qu, W. Chen, Y. L. J. Ge, Y. Yao, R. Sun, Y. Wu, L. Gu, X. Hong and Y. Li, *Nat. Commun.*, 2019, **10**, 4855.
30 D. McKeown, P. Hagans, L. L. Carette, A. Russell, K. Swider and D. Rolison, *J. Phys. Chem. B*, 1999, **103**, 4825–4832.
31 Q. Pei, J. Yu, G. Qiu, K. Tan, J. Wen, Y. Yu, J. Wang, J. Guo, J. Guo, L. Rao, T. He and P. Chen, *Appl. Catal., B*, 2023, **336**, 122947.
32 C. Zhan, Y. Xu, L. Bu, H. Zhu, Y. Feng, T. Yang, Y. Zhang, Z. Yang, B. Huang, Q. Shao and X. Huang, *Nat. Commun.*, 2021, **12**, 6261.
33 Q. Yao, B. Huang, N. Zhang, M. Sun, Q. Shao and X. Huang, *Angew. Chem., Int. Ed.*, 2019, **58**, 13983–13988.
34 J. Wang, Y. Ji, R. Yin, Y. Li, Q. Shao and X. Huang, *J. Mater. Chem. A*, 2019, **7**, 6411–6416.
35 Y. Dong, Q. Sun, C. Zhan, J. Zhang, H. Yang, T. Cheng, Y. Xu, Z. Hu, C. W. Pao, H. Geng and X. Huang, *Adv. Funct. Mater.*, 2022, **33**, 2210328.
36 R. R. Rao, M. J. Kolb, J. Hwang, A. F. Pedersen, A. Mehta, H. You, K. A. Stoerzinger, Z. Feng, H. Zhou, H. Bluhm, L. Giordano, I. E. L. Stephens and Y. Shao-Horn, *J. Phys. Chem. C*, 2018, **122**, 17802–17811.
37 H. Over, *Chem. Rev.*, 2012, **112**, 3356–3426.
38 T. F. Hsieh, C. C. Chuang, W. J. Chen, J. H. Huang, W. T. Chen and C. M. Shu, *Carbon*, 2012, **50**, 1740–1747.
39 E. Liu, L. Jiao, J. Li, T. Stracensky, Q. Sun, S. Mukerjee and Q. Jia, *Energy Environ. Sci.*, 2020, **13**, 3064–3074.
40 E. Liu, L. Jiao, J. Li, T. Stracensky, Q. Sun, S. Mukerjee and Q. Jia, *Energy Environ. Sci.*, 2020, **13**, 3064–3074.
41 L. Rebollar, S. Intikhab, J. D. Snyder and M. H. Tang, *J. Phys. Chem. Lett.*, 2020, **11**, 2308–2313.
42 B. Zhang, B. Zhang, G. Zhao, J. Wang, D. Liu, Y. Chen, L. Xia, M. Gao, Y. Liu, W. Sun and H. Pan, *Nat. Commun.*, 2022, **13**, 5894.
43 S. Zhu, X. Qin, Y. Yao and M. Shao, *J. Am. Chem. Soc.*, 2020, **142**, 8748–8754.
44 J. Kubota and K. Aika, *J. Chem. Soc., Chem. Commun.*, 1992, **8**, 661–662.
45 Z. Zhang, X. Tian, B. Zhang, L. Huang, F. Zhu, X. Qu, L. Liu, S. Liu, Y. Jiang and S. Sun, *Nano Energy*, 2017, **34**, 224–232.

46 S. Zhu, X. Qin, Y. Yao and M. Shao, *J. Am. Chem. Soc.*, 2020, **142**, 8748–8754.
47 P. Panagiotopoulou, D. I. Kondarides and X. E. Verykios, *J. Phys. Chem. C*, 2011, **115**, 1220–1230.
48 C. Fang, X. Jiang, J. Hu, J. Song, N. Sun, D. Zhang and L. Kuai, *ACS Appl. Mater. Interfaces*, 2021, **13**, 5079–5087.
49 M. J. S. Farias, W. Cheuquepán, A. A. Tanaka and J. M. Feliu, *ACS Catal.*, 2017, **7**, 3434–3445.
50 C. Elmasides, D. I. Kondarides, S. G. Neophytides and X. E. Verykios, *J. Catal.*, 2001, **198**, 195–207.
51 Z. Dong, Y. Nan, T. Tang, X.-Z. Liu, J. Fu, H.-R. Pan, Z. Jiang, L. Ding, X. Cheng, L.-R. Zheng, J. Zhang, X. Chang, B. Xu and J.-S. Hu, *ACS Catal.*, 2023, **13**, 7822–7830.
52 T. Komatsu and Y. Fukui, *Appl. Catal., A*, 2005, **279**, 173–180.